Applied Thermal Engineering 186 (2021) 116357

Contents lists available at ScienceDirect

Applied Thermal Engineering

journal homepage: www.elsevier.com/locate/apthermeng

Performance of a miniature ejector for application in a nitrogen Joule-Thomson cycle: Experimental and numerical analysis

H.S. Cao [a,b,*], L.H. Geng [a], G. Hammink [b], T. Tirolien [c], H.J.M. ter Brake [b]

[a] Key Laboratory for Thermal Science and Power Engineering of Ministry of Education, Department of Energy and Power Engineering, Tsinghua University, 100084 Beijing, China
[b] Faculty of Science and Technology, University of Twente, 7500 AE Enschede, the Netherlands
[c] European Space Agency, 2200 AG Noordwijk, the Netherlands

ARTICLE INFO

Keywords:
Ejector
Joule-Thomson effect
Cryocooler
3D printing
Turbulence modeling

ABSTRACT

The performance of Joule-Thomson (JT) cryocoolers can be improved by introducing ejectors. Ejectors with various geometric features have been proposed and investigated for cryogenic cooling in earlier studies, but only limited research is done on ejectors with a nozzle throat diameter less than 1 mm. In this paper, we present a miniature ejector with a nozzle throat diameter of 162 μm that was measured using X-ray computed tomography. When the ejector was operated with nitrogen gas at 295 K with a primary inlet pressure of 80 bar, a secondary inlet pressure of 0.5 bar and an outlet pressure of 1.2 bar, the primary and the secondary mass-flow rates were 394 mg/s and 83 mg/s, respectively. The measured primary mass-flow rate was quite close to the value predicted by a dynamic model, whereas the measured secondary mass-flow rate was lower than the predicted value, which was mainly caused by a non-axisymmetric machining defect of the nozzle that was assumed to be axisymmetric in the dynamic model. Besides, the effects of operating pressures and nozzle position on the ejector performance were analyzed. The study demonstrates the applicability of a miniature ejector in a JT cooling cycle.

1. Introduction

Joule-Thomson (JT) cryocoolers have no moving parts and are, therefore, vibration-free. These cryocoolers are attractive for cooling small optical detectors in space for earth observation and science missions. The performance of JT cryocoolers can be improved through the optimization of the working fluids and the operating pressures [1,2], the counter-flow heat exchangers (CFHXs) [3], the JT restrictions [4] and the compressors [5]. Besides the above-mentioned parameters, the performance of JT cryocoolers can also be improved by replacing the JT restrictions with work-producing devices, changing the isenthalpic expansion to an isentropic one [6]. This change will reduce the enthalpy of the working fluid entering the evaporator of JT cryocoolers and/or produce work to reduce the input power to the compressors. The work-producing devices such as turbo-expanders have moving parts, resulting in vibration. Due to the moving parts, these devices are prone to damage by low quality two-phase flow. In this study, we present the use of ejectors as work-producing devices. Ejectors use the energy of the high-pressure gas, that is completely wasted in normal JT expansion processes, to entrain and compress the low-pressure gas to an intermediate pressure. Thus, ejectors can be used to vacuumize the evaporator of JT cryocoolers, reducing the pressure of the evaporator and thereby lowering the boiling temperature of the liquid in the evaporator. This avoids the use of a room-temperature vacuum pump at subatmospheric pressure and eliminates the risk of air leakage into the system. Alternatively, ejectors can be used to lift the pressure of the flow from the evaporator to a medium pressure, thereby lowering the required input power to the compressors.

Ejectors have been widely used in various refrigeration systems to improve their performance [7]. The use of ejectors in cryogenic cooling systems was first proposed by Rietdijk [8] for creating subatmospheric pressure in a liquid helium evaporator to achieve a cooling temperature lower than 4.2 K. Afterwards, helium ejectors were further studied by Haisma [9], Nicholds [10], Agapov et al. [11], Wu et al. [12], Vonrohr and Trepp [13], Johnson and Daggett [14]. Moreover, ejectors operating with other gases, such as hydrogen gas [15] and nitrogen gas [16–19] have also been investigated. However, the above mentioned studies focused on conceptual designs or experimental investigations and only a

* Corresponding author at: Key Laboratory for Thermal Science and Power Engineering of Ministry of Education, Department of Energy and Power Engineering, Tsinghua University, 100084 Beijing, China.
E-mail addresses: HaishanCao@tsinghua.edu.cn, HaishanCao@gmail.com (H.S. Cao).

https://doi.org/10.1016/j.applthermaleng.2020.116357
Received 23 July 2020; Received in revised form 29 October 2020; Accepted 17 November 2020
Available online 9 December 2020

few studies on the theory of ejectors exist. Yu et al. [20], Rashid et al. [21] and Lee et al. [19] presented the thermodynamic analysis of the overall performance improvement due to the introduction of ejectors into cryogenic cooling systems. In these analyses, the ejector performance is estimated by using thermodynamic modeling, in which the ejector is divided into a motive nozzle, a mixing section, and a diffuser. The flow parameters including temperatures, velocities and pressures of the separate sections are obtained through mass, momentum, and energy conservation equations in each section. Detailed velocity, pressure, and temperature distributions along ejectors are not considered. The effects of frictional and mixing losses are taken into account by using corresponding coefficients introduced in the governing equations, which are usually determined by experimental results. Compared with thermodynamic modeling, dynamic modeling provides insights into the local flow physics along ejectors, which is more reliable for ejector design [22–25]. A comprehensive review on the thermodynamic and dynamic modeling can be found in our earlier study [26].

Operation parameters and geometry dimensions have significant impact on the ejector performance. As the power source of ejectors, the nozzle for a large part determines the performance of the ejector. Foroozesh et al. [27] showed that the nozzle throat diameter had more effect on the entropy generation than other geometric parameters. Yan et al. [28] concluded that an ejector with a converging-diverging nozzle had higher performance than an ejector with a converging nozzle. Moreover, the optimum geometries for the primary-flow ejector nozzle including the converging/diverging portion angle and the length were related to and varied with the nozzle exit position. The importance of the nozzle exit position was also emphasized and the optimal nozzle exit position varied with working fluids, operation parameters, mixing section diameters and nozzle throat diameters [29–31]. Although a number of numerical and experimental studies have been carried out on the ejectors, miniature ejectors with a nozzle throat diameter less than 1 mm are rarely studied, especially on the experimental investigation of such ejectors.

To provide insight into the ejector physical mechanism, this paper presents experimental and numerical studies of a miniature ejector for the application in a JT cooling cycle. In the next section, the ejector cryogenic cooling cycle is introduced. Section 3 describes the ejector geometry and fabrication, whereas the modeling and experiments are explained in Section 4. The effects of nozzle position and operating pressures on the ejector performance are discussed in Section 5. The paper is closed with conclusions in Section 6.

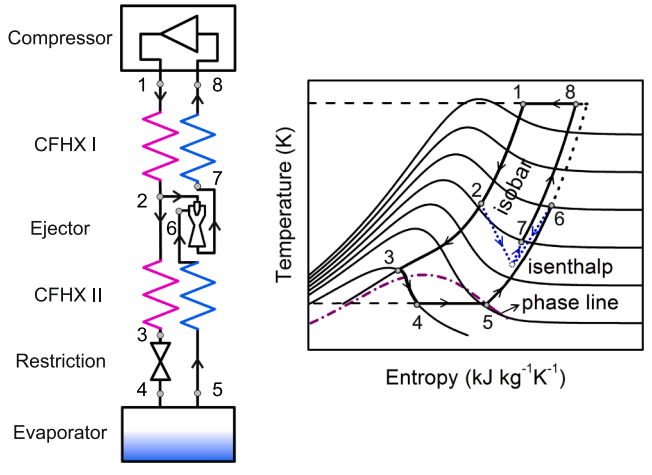

Fig. 1. Schematic of JT cooling cycle with an ejector (left) and corresponding temperature versus entropy diagram (right) [32].

2. Ejector cryogenic cooling cycle

The schematic of a typical ejector cryogenic cooling cycle and the corresponding temperature versus entropy diagram are shown in Fig. 1. In the cycle, the high-pressure gas discharged from the compressor flows through CFHX I (1→2), then it is split into two streams. One stream flowing through CFHX II (2→3) expands through the JT restriction to the evaporator (3→4). The low-pressure fluid absorbs heat from its surroundings (4→5) and flows back through CFHX II (5→6). The other stream flows to the ejector directly as the primary flow. In the ejector, the primary flow expands through the nozzle, creating a low-pressure zone, such that the secondary flow from the CFHX II is entrained into the ejector. The primary and secondary flows mix inside the ejector and the mixed flow leaves the ejector at medium pressure (2 and 6→7). The mixed flow leaving the ejector returns to the compressor through CFHX I (7→8) and cools the incoming high-pressure gas. The inlet temperatures of the ejector (points 2 and 6 shown in Fig. 1) can be adjusted by changing the size of CFHX I. In the present study, the ejector performance is considered at a temperature of 295 K.

Fig. 2 shows a schematic of a typical ejector, consisting of a nozzle, a suction chamber, a mixing section, and a diffuser. The primary flow expands through the nozzle, which results in a decrease in pressure, and an increase in velocity. The secondary flow is drawn into the ejector by the entrainment effect. In the mixing section, the velocity of the primary flow is slowed down while the secondary flow is accelerated. In the diffuser, the mixed flow is recompressed to an intermediate pressure. The global performance of an ejector is characterized by the entrainment ratio (μ), defined as the ratio of secondary mass-flow rate to primary mass-flow rate ($\dot{m}_s/\dot{m}_p$), and by the pressure lift ratio (τ), defined as the ratio of the outlet pressure of the mixed flow ($p_{m,out}$) to the secondary inlet pressure ($p_{s,in}$).

3. Ejector geometry and fabrication

The ejector geometry of our design operating with nitrogen gas is shown in Fig. 3. It has a constant pressure mixing section and a converging-diverging nozzle. The design operating parameters of the ejector are: primary flow inlet pressure 80 bar, secondary suction chamber inlet pressure 0.5 bar, outlet back pressure 1.2 bar, and inlet and outlet temperatures 295 K. The blue, red and green arrows indicate the flow direction of the primary flow, secondary flow and the outlet flow, respectively. To improve the flow distribution of the secondary flow, this flow enters the inlet and splits into two streams. The two streams enter the mixing chamber of the ejector symmetrically as shown in Fig. 3.

This design was made of titanium alloy (Ti6Al4V), consisting of nozzle and body parts as shown in Fig. 3. The body part was 3D printed with a wall roughness of about 5 μm, and the screw thread was machined afterwards. The nozzle part with a throat diameter of 162 μm (design value) was manufactured by combing mechanical machining and electrical discharge machining (EDM).

Fig. 4 shows the photograph of the nozzle part and the images of three areas of interest, obtained from X-ray computed tomography (XCT) using a GE v|*tome*|x machine. The main dimensions of the nozzle

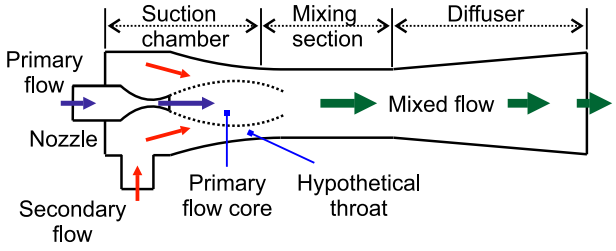

Fig. 2. Schematic of a typical ejector, adapted from [33].

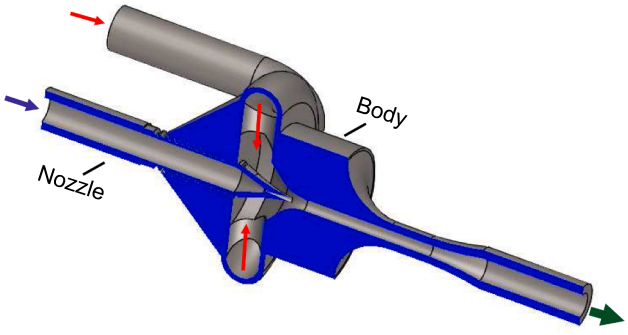

Fig. 3. Section view of the ejector design.

are shown in Fig. 4. The XCT dimensional measurements were compared against the caliper measurements. An average error of about 1.2% was calculated for all XCT measurements. Fig. 4b shows the isoview of area 1, giving the overview of the inner structure of this area. The areas 2 and 3 shown in Fig. 4c were manufactured by using EDM. The throat diameter of the nozzle is given in Fig. 4d and e, and the value is 162 μm. Fig. 4f–h show an irregular structure (machining defect) due to the EDM process. The formation of the irregular structure is probably due to particles that are eroded from the surface and got stuck to the electrode. This results in an irregular electrode and thus in a rough irregular surface.

Fig. 5 shows the photograph of the body part and the XCT images of the area of interest. The main dimensions of the body part are given in Fig. 5. Fig. 5b shows the isoview of the area of interest, giving the overview of the inner structure of this area. Figs. 5c and d show the right view and front view of this area and give the main dimensions of the inner channels.

4. Modeling and experiments

4.1. Thermodynamic model

In order to evaluate the efficiency of each part in the ejector, a thermodynamic analysis is carried out to compare with experimental results. Based on real-gas properties and the constant pressure mixing ejector model of Huang et al. [34], an ejector thermodynamic model suitable for the critical and sub-critical modes was developed and validated by Chen et al. [35]. This constant pressure mixing ejector model is used in this analysis and the detailed calculation process can be found in reference [35]. To evaluate the energy losses caused by the wall friction and the fluid viscosity, the isentropic efficiencies of nozzle and suction chamber (η_p and η_s) are used and expressed as

$$\eta_p = \frac{h_{pi} - h_{pt}}{h_{pi} - h_{pt,is}} \tag{1}$$

$$\eta_s = \frac{h_{si} - h_{st}}{h_{si} - h_{st,is}} \tag{2}$$

where h_{pi} is the fluid enthalpy at the primary nozzle inlet, h_{pt} is the fluid enthalpy at the primary nozzle throat, $h_{pt,is}$ is the enthalpy of the primary flow after isentropic expansion from the nozzle inlet to the nozzle throat, h_{si} is the fluid enthalpy at the suction chamber inlet, h_{st} is the enthalpy of the secondary flow at the hypothetical throat, and $h_{st,is}$ is the enthalpy of the secondary flow after isentropic expansion from the suction chamber inlet to the hypothetical throat.

The energy losses during the expansion process from the nozzle outlet to the hypothetical throat are represented by a coefficient ϕ_p. Furthermore, a coefficient ϕ_m is introduced to express the energy losses in the mixing section. These two coefficients are shown in the formulas below.

$$\phi_p = \frac{A_{ht,p}\rho_{ht,p}u_{ht,p}}{\dot{m}_p} \tag{3}$$

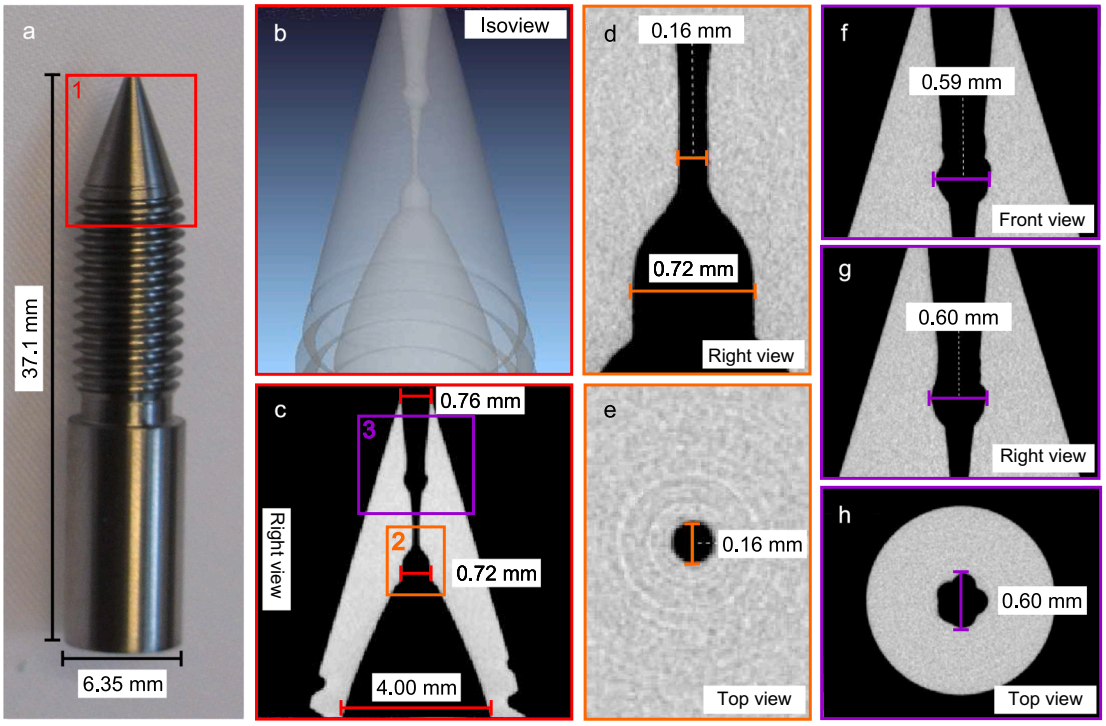

Fig. 4. Geometry of the nozzle part of the ejector. a, Photograph of the nozzle part. b-h, Images obtained from XCT. Isoview (b) and right view (c) of area 1 shown in a. Right view (d) and top view (e) of area 2 shown in c. Front view (f), right view (g) and top view of area 3 shown in c. Images f, g and h show the details of the machining defect in the nozzle.

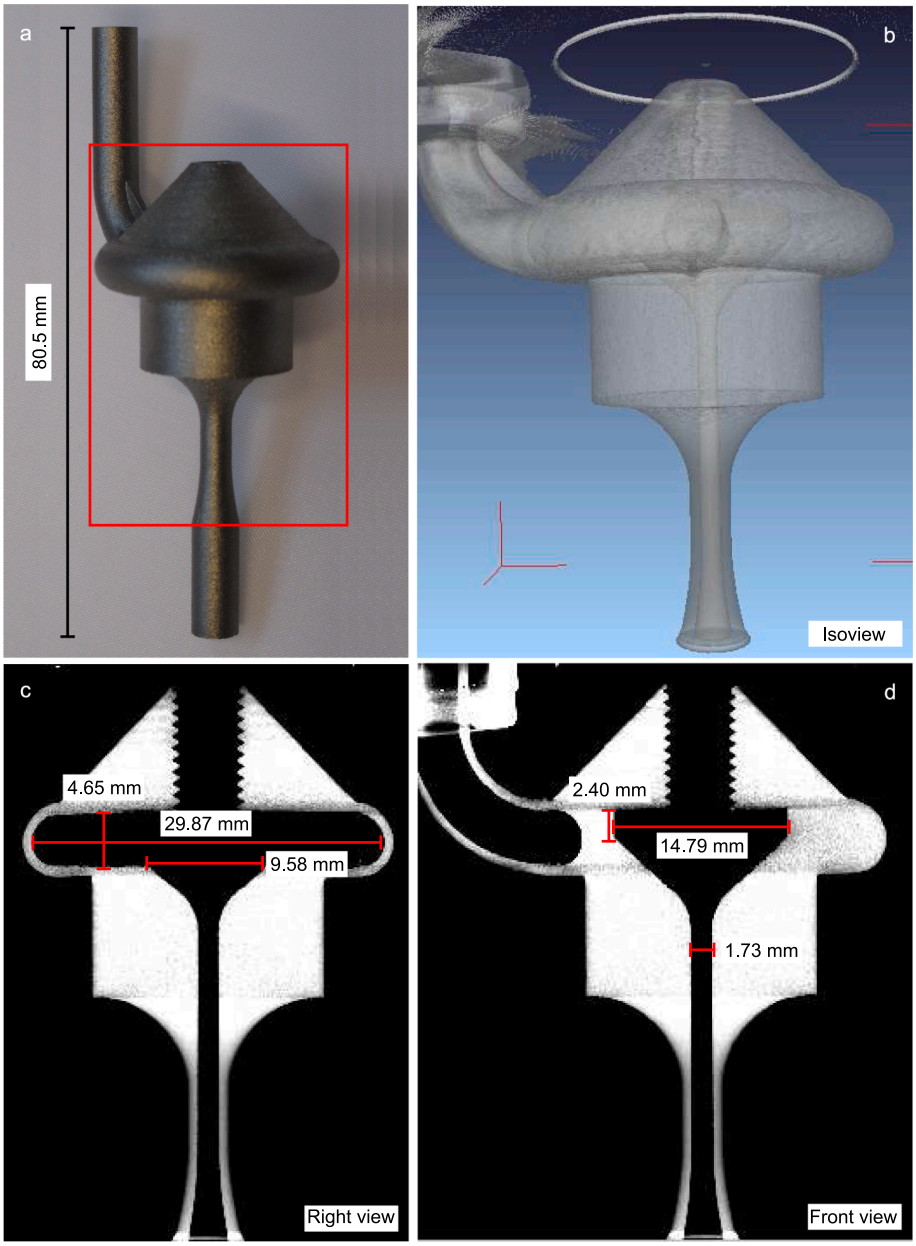

Fig. 5. Geometry of body part of the ejector. a, Photograph of the body part. b-d, Images obtained from XCT. Isoview (b), right view (c) and front view (d) of the area of interest shown in a.

$$\phi_m = \frac{(\dot{m}_p + \dot{m}_s)u_m}{(\dot{m}_p u_{ht,p} + \dot{m}_s u_{ht,s})} \tag{4}$$

where $A_{ht,p}$ is the cross-sectional area of the primary flow at the hypothetical throat, $\rho_{ht,p}$ is the density of the primary flow at the hypothetical throat, $u_{ht,p}$ is the velocity of the primary flow at the hypothetical throat, u_m is the flow velocity after complete mixing, and $u_{ht,s}$ is the velocity of secondary flow at the hypothetical throat.

4.2. CFD modeling

CFD models are adopted in this study to simulate the flow process in the ejector shown in Figs. 4 and 5. Different from thermodynamic modeling [34], CFD modeling provides insights into the local flow physics along the ejector. The flow in the ejector is typically compressible and turbulent. The governing equations (conservations of mass, momentum and energy) of the turbulent compressible flow are written as:

$$\frac{\partial \rho}{\partial t} + \frac{\partial}{\partial x_i}(\rho u_i) = 0 \tag{5}$$

$$\frac{\partial}{\partial t}(\rho u_i) + \frac{\partial}{\partial x_j}(\rho u_i u_j) = -\frac{\partial p}{\partial x_i} + \frac{\partial \tau_{ij}}{\partial x_j} \tag{6}$$

$$\frac{\partial}{\partial t}(\rho E) + \frac{\partial}{\partial x_i}(u_i(\rho E + p)) = \nabla \cdot \left(k_{eff}\frac{\partial T}{\partial x_i} + u_j \tau_{ij}\right) \tag{7}$$

where ρ is density, t is time, u is velocity, p is pressure, T is temperature, E is total energy, k_{eff} is effective thermal conductivity, and τ_{ij} is the stress tensor that is calculated by

$$\tau_{ij} = \mu_{eff}\left(\frac{\partial u_i}{\partial x_j} + \frac{\partial u_j}{\partial x_i} - \frac{2}{3}\frac{\partial u_k}{\partial x_k}\delta_{ij}\right) \tag{8}$$

where μ_{eff} is effective dynamic viscosity and δ_{ij} is the Kronecker delta

function.

4.2.1. Modeling geometry

Pianthong et al. [36] proved that the suction chamber had little influence on the flow pattern and the ejector performance obtained with a 2D axisymmetric model was very close to that of a 3D model. Therefore, the flow in the ejector is assumed to be two-dimensional, steady-state and axisymmetric, which was also recommended by other researchers for reducing computational cost [28,37]. Fig. 6 shows the detailed dimensions of the computational flow domain of the case that the nozzle exit position (NXP) is 0 mm. The dimensions are determined by the XCT measurements shown in Figs. 4 and 5. As depicted, the total length is 36.75 mm, and the nozzle throat has a radius of 81 μm and a length of 0.74 mm. The boundary conditions of the flow are the total pressure and total temperature at the primary and secondary flow inlets as well as the static pressure at the ejector outlet. The boundary conditions of the ejector wall are no slip, stationary and adiabatic. To investigate the roughness effect of the 3D printed body part on the ejector performance, the approach of "virtually shifting the wall" [38] is employed, in which an equivalent sand-grain roughness height is assumed [39,40].

4.2.2. Gas properties

The nitrogen gas properties: viscosity, specific heat, and thermal conductivity are considered as constant (1.663×10^{-5} kg m^{-1} s^{-1}, 1040.67 J kg^{-1} K^{-1}, 0.0242 W m^{-1} K^{-1}, respectively). The density of nitrogen gas is a function of the thermodynamic variables, pressure and temperature, which are related by using the Soave-Redlich-Kwong Equation of State [41].

4.2.3. Turbulence modeling

Turbulent flows are characterized by unsteady, irregular (aperiodic) motion in which transported quantities such as momentum, energy, and species concentration fluctuate in time and space. Turbulence modeling is aimed at developing tractable mathematical models that can accurately predict properties of turbulent flows. Main approaches to turbulence modeling include Reynolds Averaged Navier-Stokes (RANS) based models, Large Eddy Simulation (LES) and Direct Numerical Simulation (DNS). The amount of computational resources and efforts of LES and DNS modeling are too large for most practical applications. In this study, the RANS based models are adopted for simulating the turbulent behavior in the ejector. Time-averaged Navier-Stokes equations contain an additional term known as the Reynolds stress, which is obtained from the averaging operation over the Navier-Stokes equations to account for turbulent fluctuations in fluid momentum. Compared with other RANS based models, the SST k-ω model shows a better predicted performance in terms of local flow phenomena such as non-mixing length [42], shock wave structure [41], and static pressure distribution [43]. The SST k-ω model also has advantages in the near-wall treatment with its low-Reynolds number approach. Therefore, the SST k-ω model is used in this study. The turbulence intensity and the hydraulic diameter are used for the turbulence at the ejector inlet. A medium turbulence intensity of 5% is set for the primary and secondary inlets. The hydraulic diameters of the primary and secondary inlets are calculated from their actual geometric diameters.

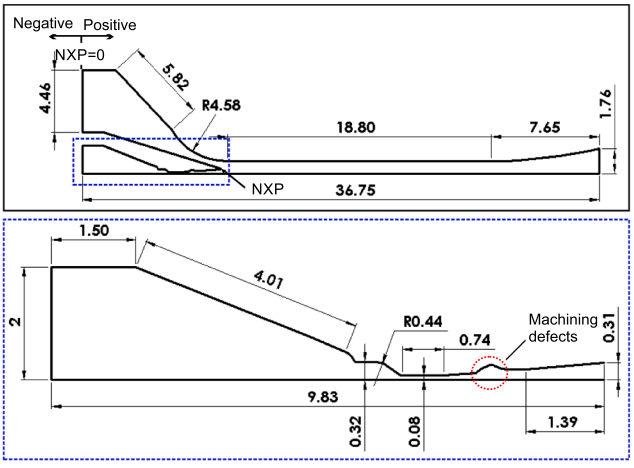

Fig. 6. Detailed dimensions of the computational flow domain (mm). The nozzle exit position (NXP) is 0 mm, and the zoomed area shows the main dimensions of the nozzle.

4.2.4. Meshing approach

For the CFD model with the flow-domain geometry as shown in Fig. 6, the high quality structured quadrilateral mesh is created using ANSYS ICEM as shown in Fig. 7. The mesh near the wall is refined to ensure correct modeling of the near-wall flow ($y^+\leqslant1$) and obtain the fluid flow characteristics in the near-wall areas. To reduce the influence of the mesh size on the calculation results and the computational cost, the grid independence is analyzed. A coarse mesh (98539 cells), two medium meshes (127119 cells, 155938 cells), a fine mesh (195794 cells) and a very fine mesh (250948 cells) are established and evaluated for the simulation. The mass-flow rate and the axial Mach number distribution are evaluated to check the solution independency from the grid densities. The Mach number distributions along the ejector axial direction for different grid densities are shown in Fig. 8. The calculated values of the mass-flow rates are shown in Table 1. It shows that variations of the primary mass-flow rate are small, whereas the secondary mass-flow rate changes under different grid densities. The relative differences of the secondary mass-flow rates calculated based on the two medium meshes is 2.5%. However, the Mach number distributions of the two medium meshes are somewhat different. Therefore, both global parameters (primary and secondary mass-flow rates, etc.) and local parameters (Mach number, pressure, etc.) are required to evaluate for the grid independence. The relative differences of the secondary mass-flow rates calculated based on the fine mesh and the very fine mesh is 1.7%. Moreover, the Mach number distribution of the fine mesh is basically coinciding with that of the very fine mesh, as shown in Fig. 8.

Three grid densities: medium mesh (127119 cells), fine mesh (195794 cells) and very fine mesh (250948 cells) are analyzed by the grid-convergence index (GCI) to obtain the discrete error due to different grid densities. The GCI can be calculated by [44,45]

$$\mathrm{GCI}=\frac{F_s|\varepsilon|}{r^p-1}\times100 \tag{9}$$

where r is the grid refinement ratio, p is the apparent order of convergence, F_s is the safety factor and ε is the relative error of calculated results between two grids.

Results of the GCI analysis, taking the secondary mass-flow rate as the parameter, are presented in Table 2. It can be found that the GCI value of Grid 1–2 is 3.65% for the secondary mass-flow rate, which indicates that discrete error due to the refinement from the fine grid to the very fine grid is small. Therefore, the fine mesh is selected to reduce the computational cost, and the corresponding grid quality is: element quality above 0.95 and orthogonal quality higher than 0.58.

4.2.5. Numerical setting

The governing equations are solved using the commercial software ANSYS Fluent 19.0, based on the finite volume method. The second order upwind scheme is used to discretize the convection term for each equation, except the pressure equation. The PRESTO! scheme is used for discretizing the convection term in the pressure equation. Gradients are evaluated by a Green-Gauss Cell Based method. The pressure-based solver based on the SIMLEC algorithm appeared to be much more stable than the density-based solvers [41] and is applied for the pressure-velocity coupling. The convergence criteria for residuals of all

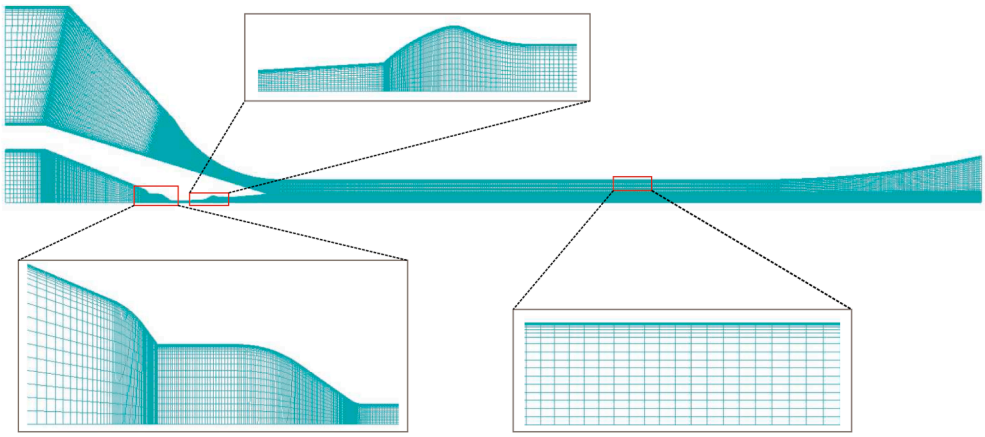

Fig. 7. The 2D axisymmetric quadrilateral grid structure of the ejector CFD model.

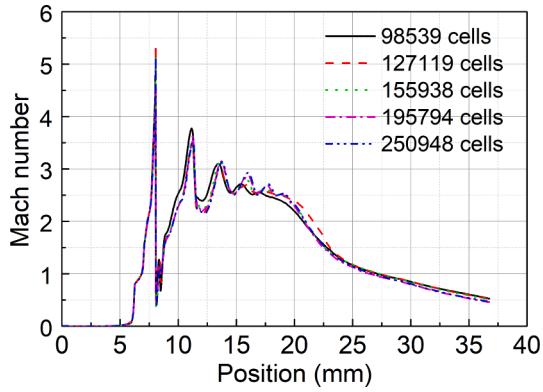

Fig. 8. Mach number distribution along the ejector axial direction for different grid densities.

Table 1
Calculated mass-flow rates based on the dynamic models with different meshes.

Cell number (–)	$\dot{m}_p$ (mg/s)	$\dot{m}_s$ (mg/s)
98539	370.0	113.4
127119	369.5	139.7
155938	371.5	136.3
195794	371.5	148.4
250948	370.3	151.0

Table 2
The grid convergence index (GCI) analysis results.

F_s	p	$\varepsilon_{1,2}$	$GCI_{1,2}$	$\varepsilon_{2,3}$	$GCI_{2,3}$
1.25	3.74	1.72	3.65	5.86	5.90

* The subscripts 1, 2, 3 represent the very fine, fine and medium meshes.

dependent variables were set to 1×10^{-5} and for the mass-flow rate imbalance between the two inlets and outlet of ejector was set to less than 1 mg/s.

4.3. Experiments

The measurement set-up is shown in Fig. 9. In the experimental setup, nitrogen gas for the primary and secondary flows is supplied from pressurized gas bottles at 295 K. The pressures and mass-flow rates of the ingoing and outgoing flows are measured. The measurement ranges of the pressure meters I, II and III are 0–100 bar, 0–1 bar, and 0–10 bar, and the measurement accuracies are ±0.5% of full scale, ±0.2% of full scale, and ±0.15% of full scale, respectively. The measurement ranges of the mass-flow meters I and II are 0.02–1 g s^{-1} and 0.04–2 g s^{-1}, and the measurement accuracies of both are ±0.5% reading plus ±0.1% full scale, respectively.

5. Results and discussion

5.1. Effect of primary inlet pressure

As shown in Fig. 10a, the secondary mass-flow rate increases with increasing primary inlet pressure. However, the slope reduces or even becomes negative at high inlet pressures. The secondary mass-flow rate decreases once the inlet pressure is greater than a critical value. This critical value increases with reducing secondary inlet pressure and increasing pressure lift ratio. For a given secondary inlet pressure and outlet pressure, the size of the hypothetical throat size reduces with the increase of primary inlet pressure, which results in an increase of secondary flow velocity at the hypothetical throat up to the speed of sound. The secondary flow correspondingly reaches the choking flow at the hypothetical throat and the entrained mass-flow rate of the secondary flow reaches its maximum value. However, if the primary inlet pressure is increased continually, the size of the hypothetical throat will be further reduced with little variations of the secondary flow velocity at the hypothetical throat, resulting in a decreasing entrained mass-flow rate accordingly. Moreover, the gradually increasing primary inlet pressure makes the position of the hypothetical throat moving away from the inlet of the mixing section, which is also unfavorable for the performance of the ejector [46], as shown in Fig. 10b. Fig. 10b shows the variation of the entrainment ratio versus the primary inlet pressure for different secondary inlet pressures. With the increase of the primary inlet pressure, the entrainment ratio increases first and then decreases due to the increase of the mass-flow rate in the primary flow and the variations of the mass-flow rate in the secondary flow. It should be noticed that the critical value of the primary inlet pressure corresponding to the maximum entrainment ratio is lower than that of the primary inlet pressure corresponding to the maximum mass-flow rates of the secondary flow.

Comparisons between the measured and predicted primary and secondary mass-flow rates at a secondary inlet pressure of 0.5 bar are carried out, as shown in Fig. 11a. Thermodynamic modeling shows that the mixing loss coefficient has much more influence than the isentropic efficiency of nozzle and suction chamber (η_p and η_s) and the loss coefficient of the primary flow expansion process after the nozzle outlet (ϕ_p), which are selected as $\eta_p = 1, \eta_s = 0.85$ and $\phi_p = 0.88$ [34], respectively. Results of the dynamic models are performed based on the ejector with

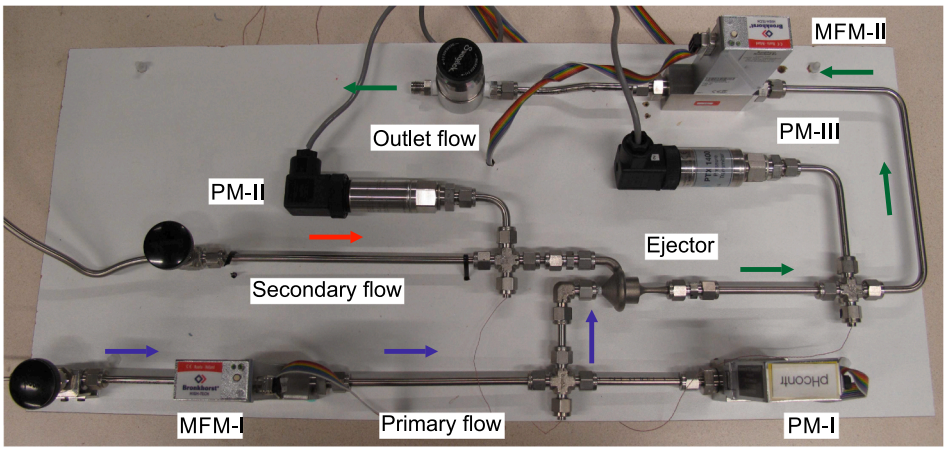

Fig. 9. The measurement set-up used for the characterization of ejectors at room temperature. (MFM: mass-flow meter; PM: pressure meter).

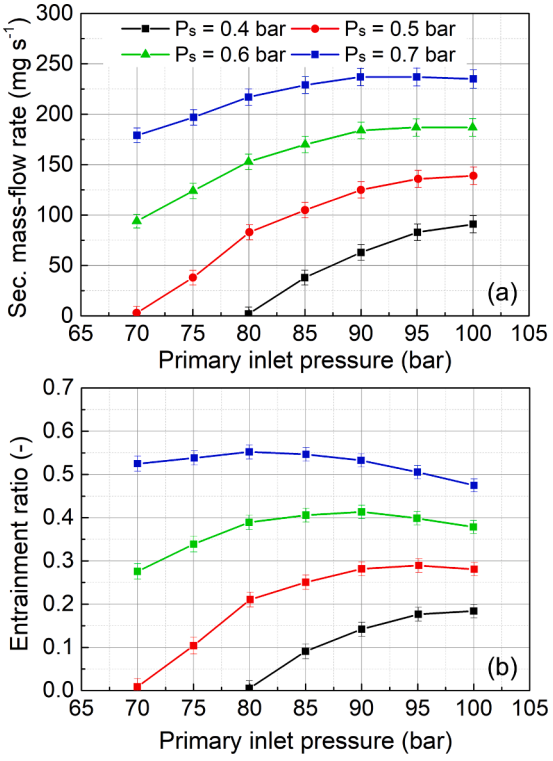

Fig. 10. (a) Effect of the primary inlet pressure on the measured secondary mass-flow rate for different secondary inlet pressures; (b) Effect of the primary inlet pressure on the entrainment ratio for different secondary inlet pressures; The outlet pressure of the ejector is 1.2 bar and the nozzle exit position is 0 mm.

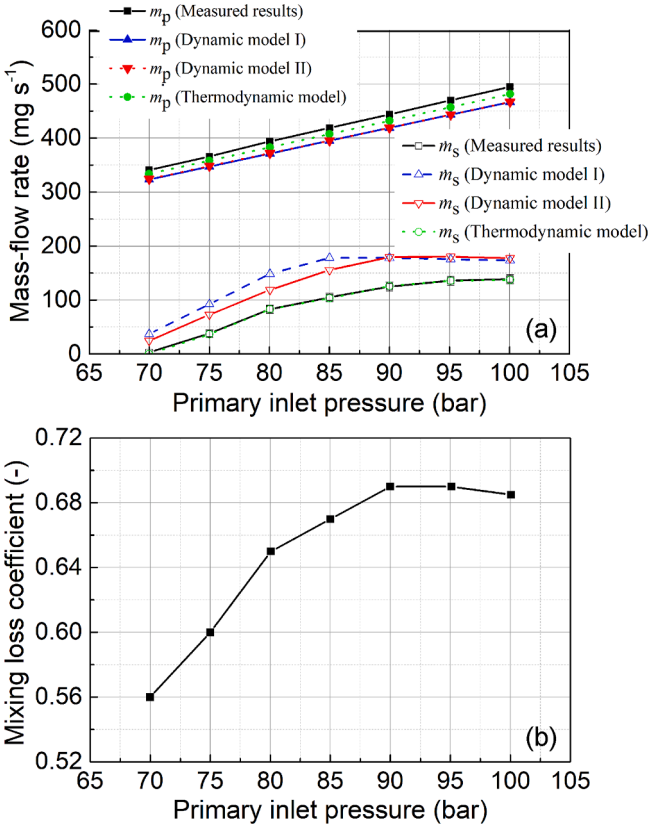

Fig. 11. (a) Comparison between the measured and predicted primary and secondary mass-flow rates at a secondary inlet pressure of 0.5 bar; (b) Variations of the mixing loss coefficient with the primary inlet pressure; The outlet pressure of the ejector is 1.2 bar and the nozzle exit position is 0 mm. In dynamic model I, the wall is assumed to be smooth; In dynamic model II, the wall roughness of the 3D printed body part is assumed to be 5 μm and the wall of the micromachined nozzle part is assumed to be smooth.

the axisymmetric machining defect. It shows that the primary mass-flow rate can be well predicted with both the dynamic models and thermodynamic model. It should be noted that the predicted results of the thermodynamic model with $\eta_p = 1$ is still slightly lower than the measured values, which indicates that the measured diameter of the nozzle throat is slightly smaller than the actual value. The secondary mass-flow rates predicted by the dynamic models are systematically over-predicted for the cases with a constant secondary pressure of 0.5 bar. This is probably due to discrepancies between the real and the computational dimensions of the irregular structure shown in Figs. 4h. In the model, the machining defects are assumed to be axisymmetric, but the actual irregular structure is different and that deteriorates the performance of the ejector. Fig. 11a shows that the wall roughness affects the ejector performance. It can be found that the secondary mass flow rates of dynamic model I are greater than that of dynamic model II when the primary inlet pressures are lower than 90 bar. As the primary inlet pressure is higher than 90 bar, the secondary mass flow rates of dynamic models I and II are approximately equal. This is because the ejector with primary inlet pressures lower than 90 bar operates at the subcritical mode, and the secondary mass flow rates increase with the increasing primary flow velocities, however, the wall roughness decreases the flow

velocities and thus the secondary mass flow rates. When the primary inlet pressures are higher than 90 bar, the flow velocities reach the speed of sound and the wall roughness effects on the flow velocities and the secondary mass flow rates are not significant. The predicted secondary mass-flow rates of the thermodynamic model are in good agreement with the experimental values by adjusting the mixing loss coefficient.

Fig. 11b presents variations of the mixing loss coefficient versus the primary inlet pressure at a constant secondary pressure of 0.5 bar. It can be seen that the mixing loss coefficient increases first and then decreases with increasing primary inlet pressure, which is similar to the variation trend of the entrainment ratio. As the primary inlet pressure increases from 70 bar to 100 bar, the mixing loss coefficient changes between 0.56 and 0.685. This is apparently lower than the recommended values in references [34,35]. Therefore, the machining defects in the nozzle diverging part of the ejector have an important impact on the mixing process of the primary and secondary flows.

Figs. 12a and b show the Mach number distribution inside the ejector with and without the machining defect. The machining defect is non-axisymmetric in practice, whereas an axisymmetric machining defect is assumed in the 2D dynamic model. Due to the defect, a shock wave occurs as shown in Fig. 12a, which results in a Mach number distribution that is different from that inside the ejector without machining defect (see Fig. 12b), and thus it deteriorates the ejector performance. The machining defect affects the Mach number and pressure along the axis of the ejector as can be seen from Fig. 13a and b. The mass-flow rates of primary flow for the ejector with and without defect are 372 mg/s and 371 mg/s, respectively. The mass-flow rates of the secondary flow with and without defect are 119 mg/s and 202 mg/s, respectively. Compared with the ejector without machining defects, the entrainment ratio of the ejector with the axisymmetric machining defect is reduced by 41.2%. It can be found that the machining defect has little influence on the mass-flow rates of the primary flow. However, due to the shock energy losses and eddy losses in the nozzle diverging section of the ejector with the axisymmetric machining defect, the energy of the primary flow for the two fluids mixing is relatively sense. Therefore, the entrained mass-flow rates of the secondary flow with defect are relatively lower.

5.2. *Effect of secondary inlet pressure*

Fig. 14 shows that the secondary mass-flow rate increases with the secondary inlet pressure, and the slope reduces as the secondary inlet pressure gets closer to the outlet pressure (here 1.2 bar). This corresponds to the discussion in Section 5.1 that the secondary mass-flow rate increases as the secondary inlet pressure is increased and the pressure lift ratio is reduced. That is the result of a combination of the pressure at the cross-section of the hypothetical throat and the hypothetical throat size. Compared with the primary inlet pressure at 90 bar, the pressure at the cross-section of the hypothetical throat is smaller whereas the hypothetical throat size is larger at 80 bar. When the secondary inlet pressure gets below 0.9 bar, the pressure at the cross-section of the hypothetical throat predominates the secondary mass-flow rate, which explains why the secondary mass-flow rate is higher at 90 bar. For the cases of the secondary inlet pressures of 0.9 and 1.0 bar, the hypothetical throat size plays a more important role and, therefore, the effect of the primary pressure is very small (80 bar or 90 bar making no difference).

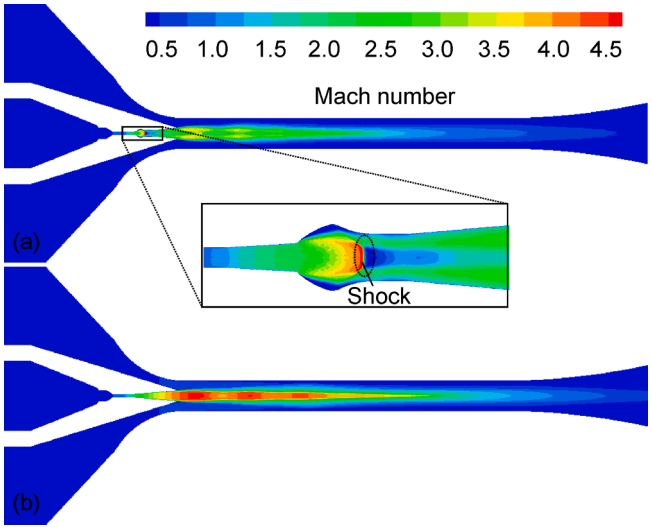

Fig. 12. Mach number distribution inside the ejector with and without the axisymmetric machining defect (a and b, respectively). The boundary conditions are: P_p=80 bar, T_p=295 K, P_s=0.5 bar, T_s=295 K and P_b= 1.2 bar. The wall roughness of the 3D printed body part is assumed to be 5 μm and the wall of the micromachined nozzle part is assumed to be smooth.

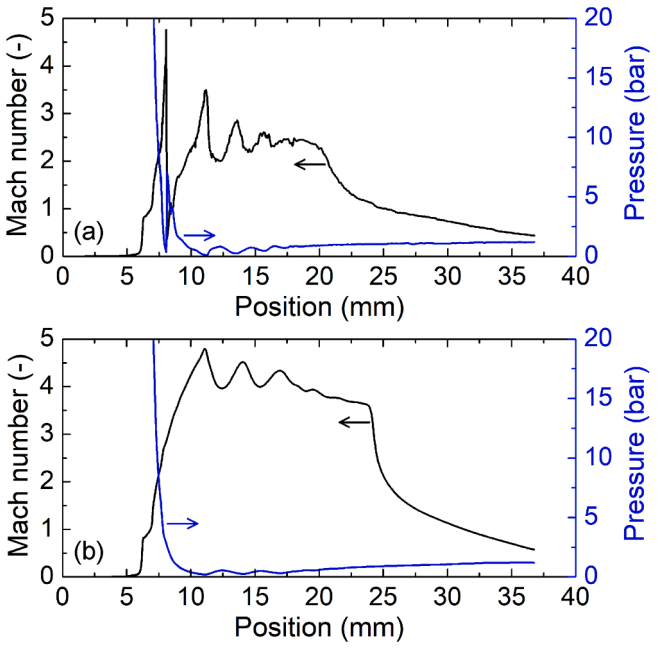

Fig. 13. Mach number and pressure along the axis of the ejector with and without the axisymmetric machining defect (a and b, respectively). The boundary conditions are: P_p=80 bar, T_p=295 K, P_s=0.5 bar, T_s=295 K and P_b= 1.2 bar. The wall roughness of the 3D printed body part is assumed to be 5 μm and the wall of the micromachined nozzle part is assumed to be smooth.

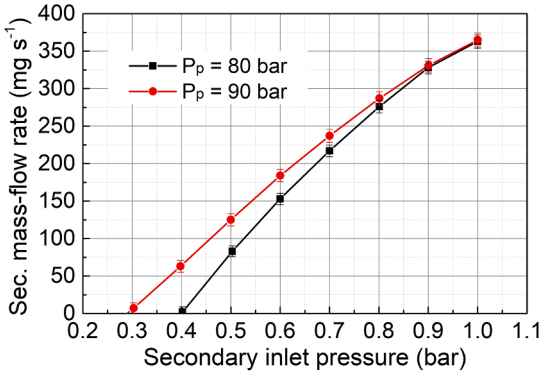

Fig. 14. Effect of the secondary inlet pressure on the secondary mass-flow rate for different primary inlet pressure. The outlet pressure of the ejector is 1.2 bar and the nozzle exit position is 0 mm.

5.3. Effect of outlet pressure

Fig. 15 shows the effect of the outlet pressure of the ejector on the secondary mass-flow rate for different secondary inlet pressures. The nozzle exit position is 0 mm and the primary inlet pressure is 80 bar, which leads to a constant mass-flow rate of the primary flow. Therefore, the variation of the secondary mass-flow rate reflects that of the entrainment ratio. It can be seen that the secondary mass-flow rate increases at lower outlet pressure and it tends to become constant as the outlet pressure is lower than a critical value. As the decrease of the ejector outlet pressure, the ejector working mode gradually changes from subcritical mode (single choked) to critical mode (double chocked). The critical value of the outlet pressure increases with increasing secondary inlet pressure, as shown in Fig. 15. When the ejector operates at the subcritical mode, the pressure at the cross section of the hypothetical throat decreases with the reduction of the outlet pressure, which results in an increase of the secondary mass-flow rate. It is worth noting that the ejector is in the subcritical mode at the designed operating parameters due to the manufactured defect. As the outlet pressure reaches its critical value (see the cases of secondary pressures at 0.8 bar and 0.9 bar), the secondary flow gets choked and the secondary mass-flow rate is only a function of the secondary inlet pressure. It is indicated that the choking flow of ejector is not only affected by the outlet pressure, but also determined by the ejector inlet conditions.

5.4. Effect of nozzle exit position

Fig. 16 shows the effect of the nozzle exit position on the secondary mass-flow rate. The primary inlet pressure and the outlet pressure of the ejector are 80 and 1.2 bar, respectively.

The primary mass-flow rate is 392 mg s^{-1}, independent of the nozzle exit position and the secondary inlet pressure. It is a function of the primary inlet pressure and the nozzle size only. The secondary mass-flow rate is determined by the secondary inlet pressure, the hypothetical throat size of the secondary flow, and the pressure at the cross section of the hypothetical throat. The hypothetical throat size is affected both by the size of the primary-flow core and the cross section of the suction-chamber where the hypothetical throat is located (see Fig. 2). The secondary mass-flow rate increases with increasing secondary inlet pressure as shown in Fig. 10. Furthermore, it increases as the nozzle exit position shifts from −5 to −2 mm. With the nozzle exit position shifting from −5 to −2 mm, the cross section of the suction-chamber decreases, and thus the increase in the secondary mass-flow rate is caused by the smaller size of the primary-flow core and/or the pressure at the cross-section of the hypothetical throat. As the nozzle exit position shifts further from −2 to 0 mm, the way in which the nozzle exit position affects the secondary mass-flow rate depends on the secondary inlet pressure. That is because the secondary inlet pressure determines how the hypothetical throat size and the pressure at the cross-section of the hypothetical throat change with the nozzle exit position.

6. Conclusions

A miniature ejector with a nozzle throat diameter of 162 μm was manufactured by means of 3D printing, mechanical machining and electrical discharge machining. The geometry of the ejector was determined using XCT. Its performance operating with nitrogen gas was investigated experimentally. The primary mass-flow rate was mainly determined by the primary pressure, whereas the secondary mass-flow rate was affected by the primary pressure, the secondary pressure, the outlet pressure and the nozzle exit position. The secondary mass-flow rate increases with increasing primary inlet pressure, increasing secondary inlet pressure and reducing outlet pressure within certain ranges. Beyond these ranges, the secondary mass-flow rate reduces instead of increases. The secondary mass-flow rate is also affected by the nozzle exit position and the optimum position depends on the operating pressures. The primary mass-flow rate can be well predicted by using the SST k-ω turbulence model, whereas the secondary mass-flow rate is systematically over-predicted due to the nonaxisymmetry of the irregular structure that is not considered in the model.

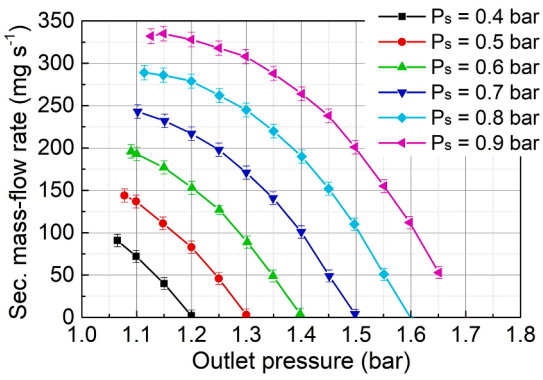

Fig. 15. Effect of the outlet pressure of the ejector on the secondary mass-flow rate for different secondary inlet pressure. The primary inlet pressure is 80 bar and the nozzle exit position is 0 mm.

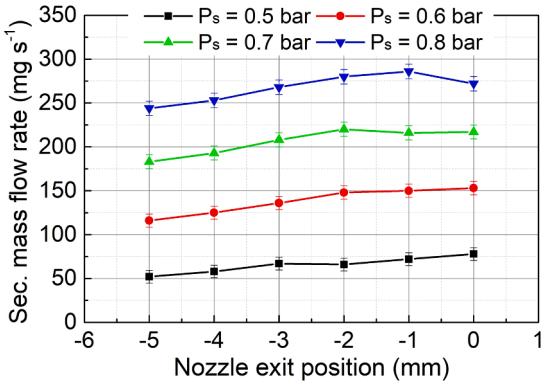

Fig. 16. Effect of the nozzle exit position on the secondary mass-flow rate for different secondary inlet pressure. The primary inlet pressure and the outlet pressure of the ejector are 80 and 1.2 bar, respectively.

Declaration of Competing Interest

The authors declare that they have no known competing financial interests or personal relationships that could have appeared to influence the work reported in this paper.

Acknowledgments

This work was supported by the National Natural Science Foundation of China (Grant No. 52076115) and the Networking/Partnering Initiative of European Space Agency (ESA) (Grant No. 4000114493/15/NL/KML/fg). We thank Martina Meisnar at ESA, for providing the X-ray computed tomography images of the ejector.

References

[1] J.H. Derking, H.J.M. ter Brake, A. Sirbi, M. Linder, H. Rogalla, Optimization of the working fluid in a Joule-Thomson cold stage, Cryogenics 49 (3) (2009) 151–157.
[2] G. Venkatarathnam, Cryogenic Mixed Refrigerant Processes, Springer, New York, 2008.
[3] H.S. Cao, S. Vanapalli, H.J. Holland, C.H. Vermeer, H.J.M. ter Brake, Heat transfer and pressure drop in microchannels with isotropically etched pillars at sub-ambient temperatures, Int. J. Refrig. 98 (2019) 334–342.
[4] B.Z. Maytal, Clog retard of a vortex throttle Joule-Thomson cryocooler: Further experimental verification, Adv. Cryo. Eng. 55 (2010) 1257–1264.

[5] S. Sobol, N. Tzabar, G. Grossman, Miniature piezoelectric compressor for Joule-Thomson cryocoolers, Phys. Procedia 67 (2015) 423–427.
[6] J.H. Park, Y.H. Kwon, Y.S. Kim, The design and fabrication of a reverse Brayton cycle cryocooler system for the high temperature superconductivity cable cooling, Cryogenics 45 (2005) 71–75.
[7] G. Besagni, Ejectors on the cutting edge: The past, the present and the perspective, Energy 170 (2019) 998–1003.
[8] J.A. Rietdijk, The expansion-ejector, a new device for liquefaction and refrigeration at 4 K and lower, Pure Appli. Cryogen. 6 (1966) 241–249.
[9] J. Haisma, Ejector in refrigerating device. Patent, US3496735A, 1970.
[10] K.E. Nicholds, Cooling apparatus of the Joule-Thomson type. Patent, US3645113, 1972.
[11] N.N. Agapov, A.I. Ageev, V.A. Belushkin, V.V. Krylov, A.G. Zel'dovich, Study of a liquid helium jet pump for circulating refrigeration systems, Cryogenics 18 (1978) 491–496.
[12] K.C. Wu, D.P. Brown, A.P. Schlafke, J.H. Sondericker, Helium refrigerator with features for operation at supercritical pressure, Adv. Cryo. Eng. 29 (1984) 495–501.
[13] P. Rudolf Von Rohr, C. Trepp, Experimental investigation of an ejector, Cryogenics 25 (1985) 684–686.
[14] D.L. Johnson, D.L. Daggett, A cold ejector for closed-cycle helium refrigerators. The Telecommunications and Data Acquisition Report, 1987, pp. 102–111.
[15] A. Lacaze, P. Gianese, Some results on hydrogen and helium ejectors, in: Proceedings of the Third International Cryogenic Engineering Conference, 1970, pp. 274–276.
[16] D.E. Daney, P.M. McConnell, T.R. Strobridge, Low-temperature nitrogen ejector performance, Adv. Cryo. Eng. 18 (1973) 476–485.
[17] W.A. Little, R.L. Paugh, Development of a fast cooldown Joule-Thomson microminiature refrigerator and vacuum package for infrared focal plane array at 70 K, Cryocoolers 6 (1991) 161–169.
[18] W.A. Litttle, Advances in Joule-Thomson cooling, Adv. Cryo. Eng. 35 (1990) 1305–1314.
[19] J. Lee, C. Lee, S. Baek, S. Jeong, Investigation of ejector-equipped Joule-Thomson refrigerator operating below 77 K, Int. J. Refrig. 78 (2017) 93–107.
[20] J. Yu, Improving the performance of small Joule-Thomson cryocooler, Cryogenics 48 (2008) 426–431.
[21] M.M. Rashidi, O. Anwar Beg, A. Habibzadeh, First and second law analysis of an ejector expansion Joule-Thomson cryogenic refrigeration cycle, Int. J. Energ. Res. 36 (2012) 231–240.
[22] N. Sharifi, M. Boroomand, M. Sharifi, Numerical assessment of steam nucleation on thermodynamic performance of steam ejectors, Appl. Therm. Eng. 52 (2) (2013) 449–459.
[23] J.G. del Valle, J. Sierra-Pallares, P.G. Carrascal, F.C. Ruiz, An experimental and computational study of the flow pattern in a refrigerant ejector. Validation of turbulence models and real-gas effects, Appl. Therm. Eng. 89 (2015) 795–811.
[24] K. Zhang, X. Zhu, X. Ren, Q. Qiu, S. Shen, Numerical investigation on the effect of nozzle position for design of high performance ejector, Appl. Therm. Eng. 126 (2017) 594–601.
[25] K. Smierciew, J. Gagan, D. Butrymowicz, Application of numerical modelling for design and improvement of performance of gas ejector, Appl. Therm. Eng. 149 (2019) 85–93.
[26] H.S. Cao, H.J.M. ter Brake, Progress and challenges in utilization of ejectors for cryogenic cooling, Appl. Therm. Eng. 167 (2020) 114783.
[27] F. Foroozesh, A.B. Khoshnevis, E. Lakzian, Investigation on the effects of water steam ejector geometry in the refrigeration systems using entropy generation assessment, J. Therm. Anal. Calorim. 141 (2020) 1399–1411.
[28] J. Yan, S.Y. Li, Z. Liu, Numerical investigation on optimization of ejector primary nozzle geometries with fixed/varied nozzle exit position, Appl. Therm. Eng. 175 (2020) 115426.
[29] J. Yan, W.J. Cai, Y.Z. Li, Geometry parameters effect for air-cooled ejector cooling systems with R134a refrigerant, Renew. Energ. 46 (2012) 155–163.
[30] K.O. Shestopalov, B.J. Huang, V.O. Petrenko, O.S. Volovyk, Investigation of an experimental ejector refrigeration machine operating with refrigerant R245fa at design and off-design working conditions. Part 2. Theoretical and experimental results, Int. J. Refrig. 55 (2015) 212–223.
[31] H.J. Chen, J.H. Zhu, J. Ge, W. Lu, L.X. Zheng, A cylindrical mixing chamber ejector analysis model to predict the optimal nozzle exit position, Energy 208 (2020) 118302.
[32] H.S. Cao, S. Vanapalli, H.J. Holland, C.H. Vermeer, T. Tirolien, H.J.M. ter Brake, High-efficiency Joule-Thomson cryocoolers incorporating an ejector, Cryocoolers 19 (2016) 419–426.
[33] S. Elbel, N. Lawrence, Review of recent developments in advanced ejector technology, Int. J. Refrig. 62 (2016) 1–18.
[34] B.J. Huang, J.M. Chang, C.P. Wang, V.A. Petrenko, A 1-D analysis of ejector performance, Int. J. Refrig. 22 (1999) 354–364.
[35] W.X. Chen, C.Y. Shi, S.P. Zhang, H.Q. Chen, D.T. Chong, J.J. Yan, Theoretical analysis of ejector refrigeration system performance under overall modes, Appl. Energy 185 (2017) 2074–2084.
[36] K. Pianthong, W. Seehanam, M. Behnia, T. Sriveerakul, S. Aphornratana, Investigation and improvement of ejector refrigeration system using computational fluid dynamics technique, Energy Convers. Manag. 48 (9) (2007) 2556–2564.
[37] Y. Han, X.D. Wang, H. Sun, G.L. Zhang, L.X. Guo, J.Y. Tu, CFD simulation on the boundary layer separation in the steam ejector and its influence on the pumping performance, Energy 167 (2019) 469–483.
[38] D.V. Brezgin, K.E. Aronson, F. Mazzelli, A. Milazzo, The surface roughness effect on the performance of supersonic ejectors, Thermophys. Aeromech. 24 (2017) 553–561.
[39] F. Mazzelli, A. Milazzo, Performance analysis of a supersonic ejector cycle working with R245fa, Int. J. Refrig. 49 (2015) 79–92.
[40] T. Adams, C. Grant, H. Watson, A simple algorithm to relate measured surface roughness to equivalent sand-grain roughness, Int. J. Mech. Eng. Mechatron. 1 (2012) 66–71.
[41] S. Croquer, S. Poncet, Z. Aidoun, Turbulence modeling of a single-phase R134a supersonic ejector. Part 1: Numerical benchmark, Int. J. Refrig. 61 (2016) 140–152.
[42] Y. Bartosiewicz, Z. Aidoun, P. Desevaux, Y. Mercadier, Numerical and experimental investigations on supersonic ejectors, Int. J. Heat Fluid Fl. 26 (2005) 56–70.
[43] G. Besagni, F. Inzoli, Computational fluid-dynamics modeling of supersonic ejectors: Screening of turbulence modeling approaches, Appl. Therm. Eng. 117 (2017) 122–144.
[44] I.B. Celik, U. Ghia, P.J. Roache, C.J. Freitas, H. Coleman, P.E. Raad, Procedure for estimation and reporting of uncertainty due to discretization in CFD applications, J. Fluids Eng. 130 (2008) 078001.
[45] M. Karimi, G. Akdogan, K.H. Dellimore, S.M. Bradshaw, Quantification of numerical uncertainty in computational fluid dynamics modelling of hydrocyclones, Comput. Chem. Eng. 43 (2012) 45–54.
[46] Y. Han, X.D. Wang, A.C.Y. Yuen, A. Li, L.X. Guo, G.H. Yeoh, J.Y. Tu, Characterization of choking flow behaviors inside steam ejectors based on the ejector refrigeration system, Int. J. Refrig. 113 (2020) 296–307.